Appl. Math. Mech. -Engl. Ed., **47**(4), 883–904 (2026)

APPLIED MATHEMATICS AND MECHANICS (ENGLISH EDITION)

https://doi.org/10.1007/s10483-026-3376-6

Multi-particle mass sensing based on a single-walled carbon nanotube resonator*

Jie WANG[1,2], Yin ZHANG[1,2,†]

1. State Key Laboratory of Nonlinear Mechanics (LNM), Institute of Mechanics,
Chinese Academy of Sciences, Beijing 100190, China;
2. School of Engineering Science, University of Chinese Academy of Sciences,
Beijing 100049, China

(Received Nov. 10, 2025 / Revised Feb. 9, 2026)

Abstract Based on the Timoshenko beam theory, a model for mass resonator sensor to detect multiple particles is developed. For a beam made of single-walled carbon nanotube (SWCNT), the nonlocal effects are incorporated in the governing equations. The approximate analytical solution for the resonance frequency of the system is derived by assuming that the mass of the adsorbed particles is much smaller than that of the system. The mass and position parameters of the multiple adsorbed particles are decoupled to establish an efficient detection method utilizing resonant frequency shifts. The identification process for the doubly clamped beam is systematically analyzed in numerical simulations. In addition, the axial force arising from temperature changes is incorporated into the beam model. The robustness of the proposed particle detection method against noise is analyzed. The model and analytical framework presented in this study provide a theoretical guideline for the design of nanoscale mass resonator sensors and particle mass detection under thermomechanical coupling conditions.

Key words mass identification, nonlocal effect, carbon nanotube (CNT), multiple particle

Chinese Library Classification O321, O341
2020 Mathematics Subject Classification 35R30, 74K10

1 Introduction

Since their discovery by Iijima in 1991[1], carbon nanotubes (CNTs) have attracted researchers from diverse fields as promising candidates for various nanodevices[2–4]. Owing to their low mass density and high stiffness[5], CNTs exhibit high resonant frequencies and have been widely employed in mass resonator sensors[6–7]. Moreover, the excellent conductivity of

---

* Citation: WANG, J. and ZHANG, Y. Multi-particle mass sensing based on a single-walled carbon nanotube resonator. *Applied Mathematics and Mechanics* (*English Edition*), **47**(4), 883–904 (2026) https://doi.org/10.1007/s10483-026-3376-6

† Corresponding author, E-mail: zhangyin@lnm.imech.ac.cn

Project supported by the Strategic Priority Research Program of Chinese Academy of Sciences (Nos. XDB0620101 and XDB0620103)

CNTs allows different-order modes of CNT-based resonators to be excited by adjusting the electrostatic actuation voltage[8]. Furthermore, CNT-based resonators can achieve both ultra-high quality factors and ultra-high sensitivity by lowering the ambient temperature[9] and employing the current-induced cleaning process[10].

Experimentation, atomistic simulation, and continuum mechanics are the established approaches for characterizing the mechanical properties of nanoscale systems[11–12]. However, each approach faces specific challenges. Experimentation requires establishing precise test parameters for diverse materials, structures, and boundary conditions, which can be difficult[13]. Similarly, atomistic simulation requires the precise specification of defects[14] and reliable empirical potential function[15] to ensure the accuracy of the results. Given these limitations associated with experimentation and atomistic simulation, the continuum mechanics approach is frequently adopted as an effective alternative[16–18]. To characterize the size dependence of structures at the nanoscale, the introduction of nonlocal theory is necessary[19]. In the nonlocal theory, the stress at a point is assumed to depend on the strains at all other points within the domain[20]. Based on the nonlocal Euler-Bernoulli beam (EBB) model, Wang and Zhang[21] studied the nonlinear chaotic vibrations of a cantilevered CNT under thermomagnetic loads. Zeng et al.[22] investigated the influence of environmental noise on the nonlinear vibrations of nonlocal CNTs, with results validated with the Runge-Kutta method. Mawphlang and Patra[23] analyzed the bending behavior of nonlocal CNTs under uniformly distributed loads with cantilever boundary conditions, and demonstrated that the nonlocal parameters exhibit a more significant effect on CNTs with small aspect ratios. Li et al.[24] employed nonlocal integral models to investigate the effects of nonlocal parameters on the natural frequencies of multi-walled carbon nanotubes (MWCNTs).

Mass resonator sensors operate by means of detecting the resonance frequency shifts caused by added mass[25]. The high sensitivity of the resonance frequency in a resonator to both the mass and position of the attached mass enables high-precision mass detection[26–27]. Zhang and Zhao[28] detected two resonance frequencies of the drum resonator, and successfully identified both the mass and position of a single adsorbate. Heinrich and Dufour[29] investigated the effects of adsorbate position, mass, moment of inertia, and eccentricity on resonance frequencies in Bernoulli-Euler beams, and evaluated the feasibility of identifying adsorbate geometry through multimodal frequency responses. Through mass sensing on CNTs with position-fixed adsorbates, Li et al.[30] realized the mass identification at the zeptogram level ($1\,\mathrm{zg} = 1 \times 10^{-24}\,\mathrm{kg}$). In practical applications, the adsorption of multiple particles on the resonator is more common than that of a single particle[31]. In addition, multi-particle detection presents more challenges than single-particle detection because of more unknowns, and the accuracy of the identification results depends on both the initial value estimates and the robustness of the algorithm[32]. Dohn et al.[33] developed a multi-particle identification method for a cantilever, but neglected the rotational inertia and shear deformation of the system. Wei and Zhang[34] proposed an iterative algorithm for the multi-particle mass identification of a doubly-clamped beam, demonstrating that inaccurate initial guesses yield erroneous results. Ma et al.[35] developed a genetic algorithm to detect multiple particles adsorbed on a microplate, but the algorithm relies on sequential particle loading.

Owing to the stochastic nature of the particle number in a single adsorption event, which can vary from one to several[36], a novel approach for determining the position and mass parameters of multiple adsorbed particles is presented in this study. The single-walled carbon nanotube (SWCNT)-based resonator is modeled as the nonlocal Timoshenko beam model. The identification of multiple particles requires the detection of resonance frequencies for different modes. Compared with the classical EBB model[33], the Timoshenko beam model can more accurately predict the higher-order resonance frequencies of the resonator. The reason is that higher-order modes are with shorter wavelengths and the shear deformation and rotary inertia effects can thus be significant. Therefore, the Timoshenko beam theory is adopted to better account for these phenomena[37]. The proposed mass identification method decouples the particle mass and position parameters, thus avoiding non-convergence issues caused by errors in the initial mass guesses[34]. Moreover, this approach enables the simultaneous loading of multiple particles, removing the limitation of sequential particle loading[35]. Doubly clamped boundary conditions are used for the resonator. Due to its fixed ends, a doubly-clamped beam is with a higher stiffness than those with other boundary conditions[37]. Consequently, for identical materials, this structure possesses higher resonant frequencies, resulting in a higher sensitivity[38]. Furthermore, to investigate the effects of temperature and noise in practical environments, the axial force induced by temperature variations is considered, and the impact of noise on the particle mass detection is evaluated.

2 Model development

An SWCNT resonator with adsorbed particles is depicted in Fig. 1. The number of particles adsorbed on the resonator in a single event exhibits stochasticity, even for identical analytes[36]. Therefore, all particles are assumed to be identical in type and mass m. As shown in Fig. 1, the positions of the three adsorbed particles are arbitrary, which are denoted as x_1, x_2, and x_3, respectively. Here, the length, thickness, and diameter of the SWCNT resonator are denoted by L, h, and d, respectively. Additionally, the Cartesian coordinate system is defined with its origin at the center of the left end of the SWCNT. The x-axis and z-axis are aligned along the axial and radial directions of the SWCNT, respectively, while the y-axis is perpendicular to both axes to complete the right-handed system.

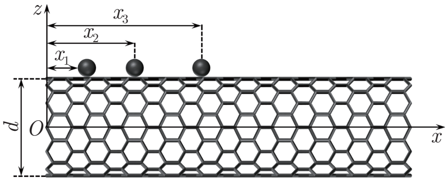

Fig. 1 Schematic of an SWCNT resonator with three adsorbed particles

To incorporate the influence of rotary inertia and shear deformation on the higher-order modes of the SWCNT resonator, the Timoshenko beam theory is adopted for the mechanical characterization of the SWCNT. Therefore, the displacement field of the system is expressed as follows[37,39]:

$$u_x = u(x,t) - z\phi(x,t), \quad u_y = 0, \quad u_z = w(x,t), \tag{1}$$

where the axial and lateral displacements are denoted by $u(x,t)$ and $w(x,t)$, respectively, while $\phi(x,t)$ represents the rotation of the cross-section.

The strain components in the Timoshenko beam theory are expressed as[37,39]

$$\varepsilon_{xx} = \frac{\partial u_x}{\partial x} + z\frac{\partial \phi}{\partial x}, \quad \gamma_{xz} = \phi + \frac{\partial w}{\partial x}. \tag{2}$$

Since the classical continuum theory fails to capture the size effects in nanostructures, Eringen's nonlocal elasticity theory[20] is implemented in this study to characterize the size-dependent behavior of the SWCNT-based mass resonator sensor. According to Eringen's theory[20], the nonlocal stress-strain correspondence is governed by the differential constitutive relation as follows:

$$\sigma_{xx} - (e_0 a)^2 \frac{\partial^2 \sigma_{xx}}{\partial x^2} = E\varepsilon_{xx}, \tag{3}$$

$$\sigma_{xz} - (e_0 a)^2 \frac{\partial^2 \sigma_{xz}}{\partial x^2} = G\gamma_{xz}, \tag{4}$$

where σ_{xx} and σ_{xz} are the non-zero stress components; E and G denote Young's modulus and shear modulus of the SWCNT, respectively; e_0 emerges as a material-specific constant; a represents the intrinsic length parameter. For SWCNTs, the nonlocal scaling parameter $e_0 a$ typically takes values within the range from 0 nm to 2 nm[40].

The resultant force N, resultant moment M, and resultant shear force Q are introduced as follows:

$$N = \int_A \sigma_{xx} \mathrm{d}A, \quad M = \int_A z\sigma_{xx} \mathrm{d}A, \quad Q = \int_A \sigma_{xz} \mathrm{d}A, \tag{5}$$

where A is the cross-sectional area. Substituting Eq. (2) into Eqs. (3) and (4) and then incorporating the resulting expressions into the last two terms of Eq. (5) yield

$$M - (e_0 a)^2 \frac{\partial^2 M}{\partial x^2} = EI \frac{\partial \phi}{\partial x}, \tag{6}$$

$$Q - (e_0 a)^2 \frac{\partial^2 Q}{\partial x^2} = K_{\mathrm{s}} GA\Big(\phi + \frac{\partial w}{\partial x}\Big), \tag{7}$$

where I and K_{s} denote the second moment of area and the shear correction coefficient, respectively. The governing equations are derived with Hamilton's principle as follows[27]:

$$\int_{t_1}^{t_2} (\delta T_{\mathrm{total}} - \delta U_{\mathrm{total}} + \delta W_{\mathrm{F}}) \mathrm{d}t = 0, \tag{8}$$

where T_{total}, U_{total}, and W_{F} denote the total kinetic energy, the total strain energy of the system, and the work done by external forces, respectively. With adsorbed particles, the total kinetic energy variation of the system can be written as follows:

$$\delta T_{\mathrm{total}} = \int_0^L \Big(\Big(\rho A + m \sum_{p=1}^{P} \delta_{\mathrm{D}}(x - x_p)\Big)\Big(\frac{\partial u}{\partial t}\delta\Big(\frac{\partial u}{\partial t}\Big) + \frac{\partial w}{\partial t}\delta\Big(\frac{\partial w}{\partial t}\Big)\Big) + \rho I \frac{\partial \phi}{\partial t}\delta\Big(\frac{\partial \phi}{\partial t}\Big)\Big)\mathrm{d}x, \tag{9}$$

where m, x_p, and P are the mass, positions, and total number of the deposited particles, respectively; ρ, t, and $\delta_{\mathrm{D}}(x - x_p)$ are the mass density of the SWCNT, the time, and the Dirac delta function with a unit of m^{-1}, respectively. As shown in Eq. (9), the adsorbed particles in this study are modeled as concentrated masses with the Dirac delta function. The concentrated mass model is with the assumption that the particle size is significantly smaller than that of a resonator[41]. For distributed masses, the Dirac delta function model, which is for the concentrated/point mass, is not applicable anymore. Furthermore, the distributed masses/particles may also result in the change of the effective stiffness of the resonator[42].

Based on Eqs. (2) and (5), the variation of the total strain energy is derived as

$$\begin{aligned} \delta U_{\mathrm{total}} &= \int_0^L \int_A (\sigma_{xx} \delta\varepsilon_{xx} + \sigma_{xz}\delta\gamma_{xz}) \mathrm{d}A \mathrm{d}x \\ &= \int_0^L \Big(N\delta\Big(\frac{\partial u}{\partial x}\Big) + m\delta\Big(\frac{\partial \phi}{\partial x}\Big) + Q\delta\Big(\frac{\partial w}{\partial x} + \phi\Big)\Big)\mathrm{d}x. \end{aligned} \tag{10}$$

In practical applications, the ambient temperature fluctuations during the operation of resonators may induce the additional axial force due to the thermal expansion mismatch between the structural components[43]. The analytical expression for this additional axial force can be formulated as follows[44]:

$$T = -\alpha EA\theta, \tag{11}$$

where α and θ represent the linear thermal expansion coefficient and the variation in ambient temperature, respectively. Under low-temperature conditions, the linear thermal expansion coefficient α is set to $-1.6 \times 10^{-6}\,\mathrm{K}^{-1}$[45]. A positive value of T denotes tension, while a negative value denotes compression. Based on Eq. (11), the variational form of W_{F} is written as

$$\delta W_{\mathrm{F}} = -\int_0^L T\frac{\partial w}{\partial x}\delta\Big(\frac{\partial w}{\partial x}\Big)\mathrm{d}x. \tag{12}$$

Substituting Eqs. (9), (10), and (12) into Eq. (8) yields

$$\delta u : \frac{\partial N}{\partial x} = \Big(\rho A + m\sum_{p=1}^{P}\delta_{\mathrm{D}}(x - x_p)\Big)\frac{\partial^2 u}{\partial t^2}, \tag{13}$$

$$\delta w : \frac{\partial Q}{\partial x} + T\frac{\partial^2 w}{\partial x^2} = \Big(\rho A + m\sum_{p=1}^{P}\delta_{\mathrm{D}}(x - x_p)\Big)\frac{\partial^2 w}{\partial t^2}, \tag{14}$$

$$\delta\phi : \frac{\partial M}{\partial x} - Q = \rho I\frac{\partial^2 \phi}{\partial t^2}. \tag{15}$$

The boundary conditions are given by

$$N|_{x=0,L} = 0 \quad \text{or} \quad u|_{x=0,L} = 0, \tag{16}$$

$$\Big(T\frac{\partial w}{\partial x} + Q\Big)\Big|_{x=0,L} = 0 \quad \text{or} \quad w|_{x=0,L} = 0, \tag{17}$$

$$M|_{x=0,L} = 0 \quad \text{or} \quad \phi|_{x=0,L} = 0. \tag{18}$$

Since the longitudinal vibration is dominated by the transverse vibration, Eq. (13) is neglected in the subsequent analysis[46]. Equations (16)–(18) each contain two distinct expressions: one specifies the natural boundary condition, and the other defines the essential boundary condition.

With Eqs. (14) and (15), the resultant moment M and resultant shear force Q in Eqs. (6) and (7) are reformulated as follows:

$$M = EI\frac{\partial\phi}{\partial x} + (e_0a)^2\Big(-T\frac{\partial^2 w}{\partial x^2} + \rho I\frac{\partial^3\phi}{\partial t^2\partial x} + \Big(\rho A + m\sum_{p=1}^{P}\delta_{\mathrm{D}}(x - x_p)\Big)\frac{\partial^2 w}{\partial t^2}\Big), \tag{19}$$

$$Q = K_{\mathrm{s}}GA\Big(\phi + \frac{\partial w}{\partial x}\Big) + (e_0a)^2\Big(-T\frac{\partial^3 w}{\partial x^3} + \Big(\rho A + m\sum_{p=1}^{P}\delta_{\mathrm{D}}(x - x_p)\Big)\frac{\partial^3 w}{\partial t^2\partial x}\Big). \tag{20}$$

Substituting Eqs. (19) and (20) into Eqs. (14) and (15) yields the governing equations for the transverse free vibration of the system as follows:

$$\begin{aligned} &K_{\mathrm{s}}GA\Big(\frac{\partial\phi}{\partial x} + \frac{\partial^2 w}{\partial x^2}\Big) + T\frac{\partial^2 w}{\partial x^2} - (e_0a)^2T\frac{\partial^4 w}{\partial x^4} \\ &= \Big(\rho A + m\sum_{p=1}^{P}\delta_{\mathrm{D}}(x - x_p)\Big)\Big(\frac{\partial^2 w}{\partial t^2} - (e_0a)^2\frac{\partial^4 w}{\partial t^2\partial x^2}\Big), \end{aligned} \tag{21}$$

$$EI\frac{\partial^2\phi}{\partial x^2} - K_{\mathrm{s}}GA\Big(\phi + \frac{\partial w}{\partial x}\Big) = \rho I\frac{\partial^2\phi}{\partial t^2} - (e_0a)^2\rho I\frac{\partial^4\phi}{\partial t^2 x^2}. \tag{22}$$

To present a general analysis, the following dimensionless parameters are introduced to nondimensionalize Eqs. (21) and (22):

$$\xi = \frac{x}{L}, \quad W = \frac{w}{L}, \quad \tau = t\sqrt{\frac{EI}{\rho A L^4}}. \tag{23}$$

Now, Eqs. (21) and (22) are written in the following the dimensionless forms:

$$\begin{aligned} & R_1\Big(\frac{\partial \phi}{\partial \xi} + \frac{\partial^2 W}{\partial \xi^2}\Big) + R_2\frac{\partial^2 W}{\partial \xi^2} - \lambda^2 R_2 \frac{\partial^4 W}{\partial \xi^4} \\ & = \Big(1 + m_{\mathrm{r}}\sum_{p=1}^{P}\delta_{\mathrm{D}}(\xi - \xi_p)\Big)\Big(\frac{\partial^2 W}{\partial \tau^2} - \lambda^2\frac{\partial^4 W}{\partial \tau^2 \partial \xi^2}\Big), \end{aligned} \tag{24}$$

$$\frac{\partial^2 \phi}{\partial \xi^2} - R_1\Big(\phi + \frac{\partial W}{\partial \xi}\Big) = R_3\frac{\partial^2 \phi}{\partial \tau^2} - \lambda^2 R_3 \frac{\partial^4 \phi}{\partial \tau^2 \xi^2}, \tag{25}$$

where ξ_p specifies the adsorption site of particle p. The dimensionless quantities in Eqs. (24) and (25) are given by

$$R_1 = \frac{K_{\mathrm{s}} G A L^2}{EI}, \quad R_2 = \frac{TL^2}{EI}, \quad R_3 = \frac{I}{AL^2}, \quad \lambda = \frac{e_0 a}{L}, \quad m_{\mathrm{r}} = \frac{m}{\rho A L}. \tag{26}$$

In Eq. (26), R_1 quantifies the ratio of shear stiffness to bending stiffness; R_2 represents the dimensionless axial force; R_3 inversely quantifies the geometric slenderness, and the condition $R_3 \ll 1$ is typically satisfied in beam structures; λ denotes the dimensionless nonlocal length; m_{r} is the mass ratio between the particle and the SWCNT.

ϕ and W are assumed in the following forms:

$$\phi(\xi, \tau) = \Phi(\xi)\mathrm{e}^{\mathrm{i}\omega\tau}, \quad W(\xi, \tau) = Y(\xi)\mathrm{e}^{\mathrm{i}\omega\tau}, \tag{27}$$

where ω represents the dimensionless frequency.

Substituting Eq. (27) into Eqs. (24) and (25) yields the governing equations as follows:

$$R_1(\Phi' + Y'') + R_2 Y'' - \lambda^2 R_2 Y'''' = \Big(1 + m_{\mathrm{r}}\sum_{p=1}^{P}\delta_{\mathrm{D}}(\xi - \xi_p)\Big)(-\omega^2 Y + \omega^2\lambda^2 Y''), \tag{28}$$

$$\Phi'' - R_1(\Phi + Y') = -\omega^2 R_3 \Phi + \omega^2 \lambda^2 R_3 \Phi'', \tag{29}$$

where $(\ )'$ denotes the partial derivative with respect to ξ. After eliminating Φ and neglecting higher-order terms associated with λ^4 because they are negligible compared with lower-order terms of λ, Eqs. (28) and (29) are decoupled into the following forms:

$$\begin{aligned} & \Big(1 + \frac{R_2}{R_1} + \lambda^2 R_2 + \omega^2\lambda^2\Big(\frac{2R_2R_3}{R_1} + R_3\Big) + \frac{\omega^2\lambda^2}{R_1}\Big(1 + m_{\mathrm{r}}\sum_{p=1}^{P}\delta_{\mathrm{D}}(\xi - \xi_p)\Big)\Big)Y'''' \\ & - \Big(R_2 - \omega^2 R_3\Big(1 + \frac{R_2}{R_1}\Big) - \omega^2\Big(\frac{1}{R_1} + \lambda^2\Big)\Big(1 + m_{\mathrm{r}}\sum_{p=1}^{P}\delta_{\mathrm{D}}(\xi - \xi_p)\Big)\Big)Y'' \\ & - \omega^2\Big(1 + m_{\mathrm{r}}\sum_{p=1}^{P}\delta_{\mathrm{D}}(\xi - \xi_p)\Big)Y = 0. \end{aligned} \tag{30}$$

When $\lambda = 0$, Eq. (30) reduces to the governing equation of the local Timoshenko beam. When $R_3 = 0$ and $R_1 \to \infty$, Eq. (30) becomes the local EBB governing equation.

The boundary conditions for both clamped-clamped (C-C) and simply supported-simply supported (S-S) beams can be derived from Eqs. (17), (18), (23), and (27) as follows:

$$Y|_{\xi=0} = 0, \quad Y|_{\xi=1} = 0, \quad Y'|_{\xi=0} = 0, \quad Y'|_{\xi=1} = 0, \tag{31}$$

$$Y|_{\xi=0} = 0, \quad Y|_{\xi=1} = 0, \quad Y''|_{\xi=0} = 0, \quad Y''|_{\xi=1} = 0. \tag{32}$$

Note that Eqs. (31) and (32) correspond to the C-C and S-S boundary conditions, respectively.

Y is assumed as follows:

$$Y(\xi) = \sum_{i=1}^{N} q_i \varphi_i(\xi), \tag{33}$$

where N, q_i, and $\varphi_i(\xi)$ denote the number of vibration modes, the modal amplitude, and the mode shape, respectively. The detailed expression of the mode shape $\varphi_i(\xi)$ for the beam with an axial load is provided in Appendix A. Substituting Eq. (33) into Eq. (32) and applying the Galerkin method to the resulting equation yield the following eigenvalue problem:

$$\boldsymbol{K}(\omega)\boldsymbol{Q} = \boldsymbol{0}, \tag{34}$$

where $\boldsymbol{Q} = (q_1, q_2, q_3, \cdots, q_N)^{\mathrm{T}}$. The element K_{ij} of the $N \times N$ matrix $\boldsymbol{K}$ is defined as follows:

$$\begin{aligned} K_{ij} &= \Big(1 + \frac{R_2}{R_1} + \lambda^2 R_2 + \omega^2 \lambda^2 \Big(\frac{1 + 2R_2R_3}{R_1} + R_3\Big)\Big) \int_0^1 \varphi_i'''' \varphi_j \mathrm{d}\xi \\ &\quad - \Big(R_2 - \omega^2 R_3 \Big(1 + \frac{R_2}{R_1}\Big) - \omega^2 \Big(\frac{1}{R_1} + \lambda^2\Big)\Big) \int_0^1 \varphi_i'' \varphi_j \mathrm{d}\xi - \omega^2 \delta_{ij} \\ &\quad + \frac{\omega^2 \lambda^2 m_{\mathrm{r}}}{R_1} \sum_{p=1}^{P} \varphi_i''''(\xi_p) \varphi_j(\xi_p) + \omega^2 \Big(\frac{1}{R_1} + \lambda^2\Big) m_{\mathrm{r}} \sum_{p=1}^{P} \varphi_i''(\xi_p) \varphi_j(\xi_p) \\ &\quad - \omega^2 m_{\mathrm{r}} \sum_{p=1}^{P} \varphi_i(\xi_p) \varphi_j(\xi_p), \end{aligned} \tag{35}$$

where δ_{ij} is the Kronecker symbol. The necessary and sufficient condition for Eq. (34) to have non-trivial solutions is $\det(\boldsymbol{K}) = 0$. This determinant condition forms the characteristic equation for ω, which can be solved numerically. When the mass resonator sensor is excited at its ith mode, the amplitude q_i of this mode becomes significantly larger than those of other modes. If the relative mass ratio of the adsorbed particles is sufficiently small ($m_{\mathrm{r}} < 0.01$), the off-diagonal elements in $\boldsymbol{K}$ can be neglected[47]. Consequently, $\det(\boldsymbol{K}) = 0$ is reduced to

$$\begin{aligned} & m_{\mathrm{r}} \Big(\sum_{p=1}^{P} \varphi_i(\xi_p) \varphi_i(\xi_p) - \frac{\lambda^2}{R_1} \sum_{p=1}^{P} \varphi_i''''(\xi_p) \varphi_i(\xi_p) - \Big(\frac{1}{R_1} + \lambda^2\Big) \sum_{p=1}^{P} \varphi_i''(\xi_p) \varphi_i(\xi_p) \Big) \\ &= \frac{1 + \frac{R_2}{R_1} + \lambda^2 R_2 + \omega_i^2 \lambda^2 \Big(\frac{1 + 2R_2R_3}{R_1} + R_3\Big)}{\omega_i^2} \int_0^1 \varphi_i'''' \varphi_i \mathrm{d}\xi \\ &\quad - \frac{R_2 - \omega_i^2 R_3 \Big(1 + \frac{R_2}{R_1}\Big) - \omega_i^2 \Big(\frac{1}{R_1} + \lambda^2\Big)}{\omega_i^2} \int_0^1 \varphi_i'' \varphi_i \mathrm{d}\xi - 1. \end{aligned} \tag{36}$$

When dealing with larger particle masses, the resonator needs to appropriately increase its own mass to reduce the relative mass ratio m_{r}, thereby maintaining the validity of Eq. (36). As shown below, the calculation results based on Eq. (36) indicate that the resonant frequency of the resonator decreases when particles are adsorbed onto it. The reason is that the present work primarily considers the mass effect on the resonant frequency[36]. However, it has been found that the adsorption of Escherichia coli (E. coli) bacteria[48] or ethyl acetate[49] can increase the resonant frequency of the resonator. The reason is that biological/chemical adsorption not only induces the mass effect but also significantly increases the effective stiffness of the resonator. Therefore, the model in the current study is applicable only to the adsorption cases where the mass effect dominates.

3 Identification of the particle mass

Jensen et al.[36] measured the mass of a single gold atom by detecting the resonance frequency shift of a CNT. Their results show that multiple atoms can be adsorbed simultaneously in a single event. Such a scenario represents a direct application for the algorithm developed in this study. Hence, the adsorbed particles are assumed to have identical masses. This assumption is crucial to decouple mass and position parameters, thereby eliminating the need for initial mass estimation. In mass resonator sensor applications, resonant frequencies are the known/measured parameters, and the total number of particles can be determined using a scanning electron microscope[34], whereas the adsorbed particle mass is unknown. The adsorption position is another unknown owing to the inherent randomness of particle locations[33]. Therefore, determining both the masses and positions of the adsorbed P particles requires at least $P+1$ resonant frequency measurements. Now, the eigenfrequencies derived from $\det(\boldsymbol{K})=0$ are assumed to correspond to the experimentally measured resonant frequencies. To determine the mass and position of a single particle adsorbed on the resonator sensor, the following two equations derived from Eq. (36) are used:

$$\begin{aligned}&m_{\mathrm{r}}\Big(\varphi_1(\xi_1)\varphi_1(\xi_1)-\frac{\lambda^2}{R_1}\varphi_1''''(\xi_1)\varphi_1(\xi_1)-\Big(\frac{1}{R_1}+\lambda^2\Big)\varphi_1''(\xi_1)\varphi_1(\xi_1)\Big)\\&=\frac{1+\frac{R_2}{R_1}+\lambda^2R_2+\omega_1^2\lambda^2\Big(\frac{1+2R_2R_3}{R_1}+R_3\Big)}{\omega_1^2}\int_0^1\varphi_1\varphi_1\mathrm{d}\xi\\&\quad-\frac{R_2-\omega_1^2R_3\Big(1+\frac{R_2}{R_1}\Big)-\omega_1^2\Big(\frac{1}{R_1}+\lambda^2\Big)}{\omega_1^2}\int_0^1\varphi_1''\varphi_1\mathrm{d}\xi-1,\end{aligned}\tag{37}$$

$$\begin{aligned}&m_{\mathrm{r}}\Big(\varphi_2(\xi_1)\varphi_2(\xi_1)-\frac{\lambda^2}{R_1}\varphi_2''''(\xi_1)\varphi_2(\xi_1)-\Big(\frac{1}{R_1}+\lambda^2\Big)\varphi_2''(\xi_1)\varphi_2(\xi_1)\Big)\\&=\frac{1+\frac{R_2}{R_1}+\lambda^2R_2+\omega_2^2\lambda^2\Big(\frac{1+2R_2R_3}{R_1}+R_3\Big)}{\omega_2^2}\int_0^1\varphi_2''''\varphi_2\mathrm{d}\xi\\&\quad-\frac{R_2-\omega_1^2R_3\Big(1+\frac{R_2}{R_1}\Big)-\omega_2^2\Big(\frac{1}{R_1}+\lambda^2\Big)}{\omega_2^2}\int_0^1\varphi_2''\varphi_2\mathrm{d}\xi-1,\end{aligned}\tag{38}$$

where ω_1 and ω_2 are the first and second eigenfrequencies, respectively; ξ_1 is the position of the particle. For convenience, Eqs. (37) and (38) are expressed in the following simplified forms:

$$m_{\mathrm{r}}F_1(R_1,\lambda,\xi_1)=G_1(R_1,R_2,R_3,\lambda,\omega_1),\tag{39}$$

$$m_{\mathrm{r}}F_2(R_1,\lambda,\xi_1)=G_2(R_1,R_2,R_3,\lambda,\omega_2).\tag{40}$$

Note that Eqs. (39) and (40) contain both the mass and position parameters of the particle, so direct solving may require a robust fitting procedure[33]. The main challenge is that solving Eqs. (39) and (40) requires initial guesses for both particle mass and position. Poor guesses can yield incorrect results or results failed to converge[34]. Additionally, as the number of attached particles increases, the complexity of the fitting procedure and the solution time also increase. To eliminate the need for guessing the initial particle mass and enhance the computational efficiency, Eqs. (39) and (40) can be decoupled by eliminating m_{r}, yielding the following expression:

$$\frac{F_2(R_1,\lambda,\xi_1)}{F_1(R_1,\lambda,\xi_1)}=\frac{G_2(R_1,R_2,R_3,\lambda,\omega_2)}{G_1(R_1,R_2,R_3,\lambda,\omega_1)}. \tag{41}$$

Therefore, the identification of a single particle on the resonator can be achieved by first determining its position ξ_1 using Eq. (41) and then substituting the resulting ξ_1 into Eq. (39) or (40) to calculate the particle mass m_{r}.

When P particles are adsorbed on the resonator sensor, the following system of equations is derived based on Eq. (36):

$$\begin{cases}\dfrac{F_2(R_1,\lambda,\xi_1,\xi_2,\cdots,\xi_P)}{F_1(R_1,\lambda,\xi_1,\xi_2,\cdots,\xi_P)}=\dfrac{G_2(R_1,R_2,R_3,\lambda,\omega_2)}{G_1(R_1,R_2,R_3,\lambda,\omega_1)},\\ \dfrac{F_3(R_1,\lambda,\xi_1,\xi_2,\cdots,\xi_P)}{F_1(R_1,\lambda,\xi_1,\xi_2,\cdots,\xi_P)}=\dfrac{G_3(R_1,R_2,R_3,\lambda,\omega_3)}{G_1(R_1,R_2,R_3,\lambda,\omega_1)},\\ \qquad\qquad\vdots\\ \dfrac{F_{P+1}(R_1,\lambda,\xi_1,\xi_2,\cdots,\xi_P)}{F_1(R_1,\lambda,\xi_1,\xi_2,\cdots,\xi_P)}=\dfrac{G_{P+1}(R_1,R_2,R_3,\lambda,\omega_{P+1})}{G_1(R_1,R_2,R_3,\lambda,\omega_1)}.\end{cases} \tag{42}$$

The multi-particle identification process is outlined as follows. After the resonant frequencies of the resonator sensor with multiple particles are determined by $\det(\boldsymbol{K})=0$, Eq. (42) is solved to obtain the position parameters of all the particles. These parameters can then be substituted into any one of the following equations in the system to calculate the particle mass m_{r}:

$$\begin{cases}m_{\mathrm{r}}F_1(R_1,\lambda,\xi_1,\xi_2,\xi_3,\cdots,\xi_P)=G_1(R_1,R_2,R_3,\lambda,\omega_1),\\ m_{\mathrm{r}}F_2(R_1,\lambda,\xi_1,\xi_2,\xi_3,\cdots,\xi_P)=G_2(R_1,R_2,R_3,\lambda,\omega_2),\\ \qquad\qquad\vdots\\ m_{\mathrm{r}}F_{P+1}(R_1,\lambda,\xi_1,\xi_2,\xi_3,\cdots,\xi_P)=G_{P+1}(R_1,R_2,R_3,\lambda,\omega_{P+1}).\end{cases} \tag{43}$$

4 Results and discussion

In this section, the following material and geometric parameters for the SWCNT resonator are considered[43]: Poisson's ratio $\nu=0.3$, Young's modulus $E=1\,\mathrm{TPa}$, the shear correction factor $K_{\mathrm{s}}=10/9$, the effective thickness $h=0.35\,\mathrm{nm}$, and the diameter $d=0.7\,\mathrm{nm}$.

4.1 Validation of the results

To enable a comparative analysis with existing literature for validating the correctness and reliability of the current model and results, Eq. (36) is reformulated as follows:

$$\begin{aligned}\omega_i^2=&\frac{\Big(1+\frac{R_2}{R_1}+\lambda^2R_2+\omega_i^2\lambda^2\Big(\frac{1+2R_2R_3}{R_1}+R_3\Big)\Big)\int_0^1\varphi_i\varphi_i\mathrm{d}\xi}{m_{\mathrm{r}}\Big(\sum\limits_{p=1}^{P}\varphi_i(\xi_p)\varphi_i(\xi_p)-\frac{\lambda^2}{R_1}\sum\limits_{p=1}^{P}\varphi_i''''(\xi_p)\varphi_i(\xi_p)-\Big(\frac{1}{R_1}+\lambda^2\Big)\sum\limits_{p=1}^{P}\varphi_i''(\xi_p)\varphi_i(\xi_p)\Big)+1}\\ &-\frac{\Big(R_2-\omega_i^2R_3\Big(1+\frac{R_2}{R_1}\Big)-\omega_i^2\Big(\frac{1}{R_1}+\lambda^2\Big)\Big)\int_0^1\varphi_i''\varphi_i\mathrm{d}\xi}{m_{\mathrm{r}}\Big(\sum\limits_{p=1}^{P}\varphi_i(\xi_p)\varphi_i(\xi_p)-\frac{\lambda^2}{R_1}\sum\limits_{p=1}^{P}\varphi_i''''(\xi_p)\varphi_i(\xi_p)-\Big(\frac{1}{R_1}+\lambda^2\Big)\sum\limits_{p=1}^{P}\varphi_i''(\xi_p)\varphi_i(\xi_p)\Big)+1}.\end{aligned} \tag{44}$$

When neglecting the adsorbed particles, Eq. (44) is reduced to

$$\begin{aligned}\omega_{i,0}^2 &= \Big(1+\frac{R_2}{R_1}+\lambda^2 R_2+\omega_i^2\lambda^2\Big(\frac{1+2R_2R_3}{R_1}+R_3\Big)\Big)\int_0^1 \varphi_i\varphi_i\mathrm{d}\xi \\ &\quad -\Big(R_2-\omega_i^2 R_3\Big(1+\frac{R_2}{R_1}\Big)-\omega_i^2\Big(\frac{1}{R_1}+\lambda^2\Big)\Big)\int_0^1 \varphi_i''\varphi_i\mathrm{d}\xi. \qquad (45)\end{aligned}$$

Based on Eqs. (44) and (45), the influence of the attached particles on the resonant frequencies of the system is mathematically expressed by

$$R_i = m_{\mathrm{r}}\Big(\sum_{p=1}^{P}\varphi_i(\xi_p)\varphi_i(\xi_p)-\frac{\lambda^2}{R_1}\sum_{p=1}^{P}\varphi_i''''(\xi_p)\varphi_i(\xi_p)-\Big(\frac{1}{R_1}+\lambda^2\Big)\sum_{p=1}^{P}\varphi_i''(\xi_p)\varphi_i(\xi_p)\Big), \qquad (46)$$

where $R_i = \omega_{i,0}^2/\omega_i^2 - 1$.

Consider a doubly clamped SWCNT with three particles of equal mass $m_{\mathrm{r}} = 0.0005$, attached at $\xi_1 = 0.224$, $\xi_2 = 0.376$, and $\xi_3 = 0.576$. The R_i values obtained from the proposed model without nonlocal effects, Dohn et al.'s model[33], and Wei and Zhang's model[34] are compared in Fig. 2(a). As shown in Fig. 2(a), the results obtained from the proposed model agree perfectly with those given by Dohn et al.'s model[33] and Wei and Zhang's model[34].

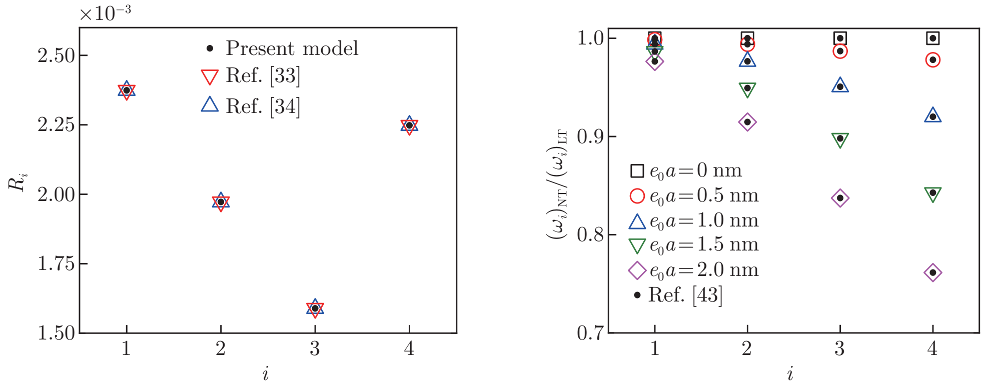

(a) Comparison of R_i under the C-C boundary conditions ($L=20d$, $\theta=0$ K, $\lambda=0$)

(b) Comparison of $(\omega_i)_{\mathrm{NT}}/(\omega_i)_{\mathrm{LT}}$ under the S-S boundary conditions ($L=40d$, $\theta=40$ K)

Fig. 2 Comparison of current results with those in Refs. [33], [34], and [43] (color online)

The comparison between the normalized dimensionless frequencies obtained in this study and those from Ref. [43] under the S-S boundary conditions is presented in Fig. 2(b), where $(\omega_i)_{\mathrm{NT}}$ and $(\omega_i)_{\mathrm{LT}}$ denote the resonant frequencies derived from the nonlocal Timoshenko beam model and the local Timoshenko beam model, respectively. It can be observed from Fig. 2(b) that the present results are consistent with those of Ref. [43] for various values of the nonlocal parameter e_0a.

A comparison between the results obtained in this study and those from the molecular dynamics (MD) simulations in Ref. [52] is shown in Fig. 3. The following material parameters are used in Fig. 3: Poisson's ratio $\nu = 0.19$[50], diameter $d = 0.678\,\mathrm{nm}$[50], carbon bond length $a = 0.14\,\mathrm{nm}$[50], shear correction factor $K_{\mathrm{s}} = 0.563$[51], the ratio of Young's modulus to mass density $E/\rho = 3.6481\times10^8\,\mathrm{m}^2/\mathrm{s}^2$[52], and calibration constant $e_0 = 1.25$[52]. From Fig. 3, it can been obtained that the results of the present model agree excellently with those of the MD simulations for large length-to-diameter ratios (L/d). There are some differences between the two results when the ratio of L/d is small. The reason is that the calibration constant e_0 increases notably as the aspect ratio decreases[50], making the fixed value $e_0 = 1.25$ inapplicable.

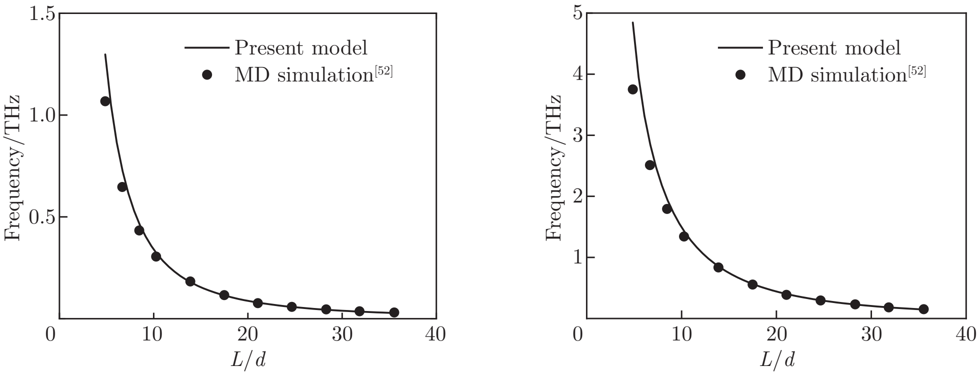

(a) Frequencies of the first mode (b) Frequencies of the third mode

Fig. 3 Comparison of the current results with those by MD simulations in Ref. [52]

4.2 Influence of different parameters on the resonator

The variations in the normalized frequencies of the SWCNT resonator as a function of the nonlocal parameter λ under the C-C boundary conditions are shown in Figs. 4(a) and 4(b). The case without axial force is presented in Fig. 4(a), while the case with an axial force $R_2 = 5$ is plotted in Fig. 4(b). As shown in Figs. 4(a) and 4(b), an increase in the axial force leads to a rise in the normalized frequencies for various modes. This phenomenon occurs because the increased axial force enhances the equivalent stiffness of the system, thereby elevating the frequencies. Additionally, the effect of axial force is most pronounced on the first normalized frequency. The normalized frequencies under both axially loaded and non-axially loaded conditions decrease as the nonlocal parameter λ increases. This indicates that accounting for the nonlocal effects reduces the effective stiffness of the system, thereby leading to a reduction in the frequencies. Furthermore, the nonlocal effect exhibits a more pronounced effect on the higher-order normalized frequencies. This suggests that the nonlocal theory should be incorporated to accurately predict higher-order resonance frequencies in CNT-based resonators. It should be noted that the nonlocal theory tends to overestimate the first natural frequency of cantilever beams, which stems from the fact that the bending vibration problem of nonlocal cantilever beams is nonself-adjoint[37,51].

Mass sensitivity is a critical performance metric in resonator characterization. It is defined as the ratio of the change in the resonance frequency ($\Delta\omega_i$) to the mass of adsorbed particles (Δm_{r}) for a given mode. The expression for the sensitivity S is given as follows:

$$S = \frac{\Delta\omega_i}{\Delta m_{\mathrm{r}}}. \tag{47}$$

The influence of particle position on the sensitivity, for the case of single-particle adsorption, is illustrated in Figs. 5(a) and 5(b). For the C-C boundary conditions, the first mode sensitivity drops to zero when the particle is positioned at the clamped ends but peaks near the resonator midpoint. In addition, zero sensitivity is observed when the particle is adsorbed at the nodes of the higher-order modes under both boundary conditions. This occurs because the vibrational amplitudes are completely suppressed at these nodes. Therefore, to enhance resonator sensitivity, it is recommended that the particles should be adsorbed at $\xi_p \in [0.2, 0.8]$ for the C-C boundary conditions. The confinement of particle attachment positions can be achieved by implementing baffles on the resonator[36]. The mass sensitivity of the resonator is enhanced by an increased axial force, as shown in Figs. 5(a) and 5(b). For example, at the particle adsorption position $\xi_p = 0.5$, the absolute value of the first mode sensitivity increases from 27.504 (with no axial force) to 31.022 (under an axial force of $R_2 = 5$).

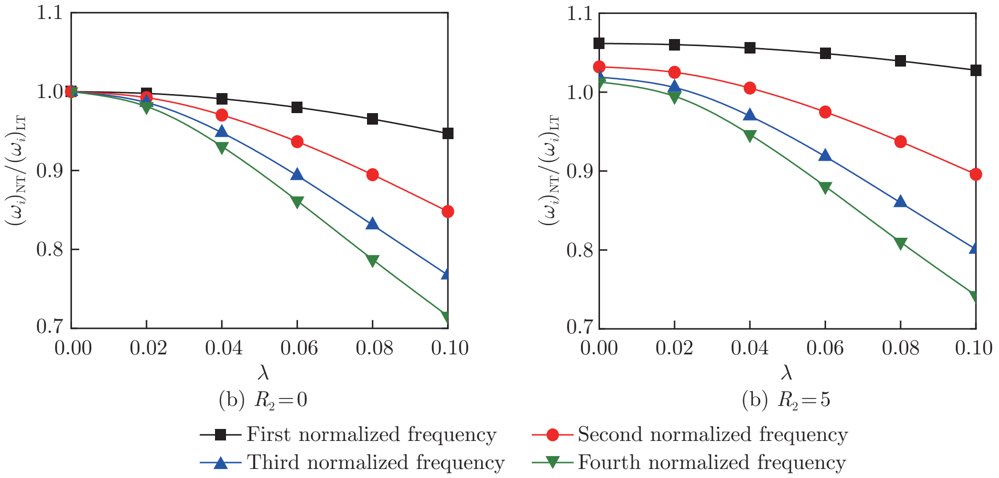

(b) $R_2=0$ (b) $R_2=5$

Fig. 4 Nonlocal effects on the normalized frequencies of the SWCNT resonator under the C-C boundary conditions when $L = 20d$ (color online)

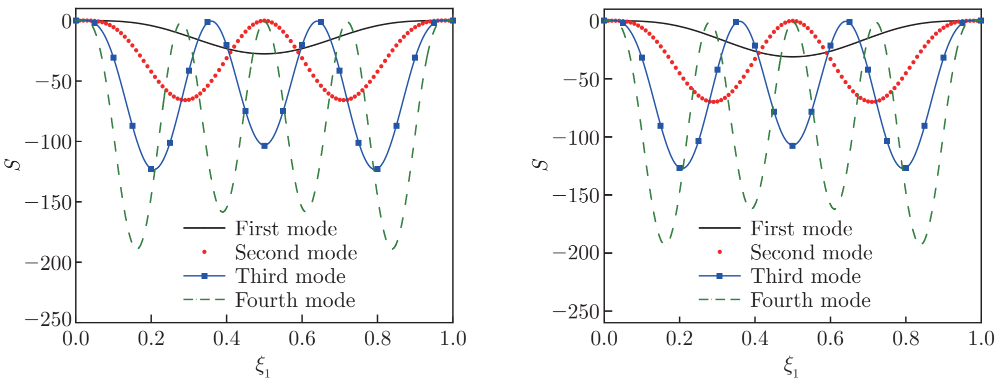

(a) $R_2=0$ (b) $R_2=5$

Fig. 5 Effects of particle adsorption position on the sensitivity when $L = 20d$ and $\lambda = 0$ (color online)

The effects of the number of adsorbed particles on the sensitivity are plotted in Fig. 6. In Figs. 6(a) and 6(b), three adsorption cases are considered: one particle with $\xi_1 = 0.2$; two particles with $\xi_1 = 0.2$ and $\xi_2 = 0.3$; three particles with $\xi_1 = 0.2$, $\xi_2 = 0.3$, and $\xi_3 = 0.4$. As displayed in Figs. 6(a) and 6(b), when the number of particles is fixed, the absolute sensitivity exhibits an increasing trend with higher modes and axial force. The nonlinear increase in the absolute sensitivity is due to the differing sensitivities of various modes to the particle adsorption positions.

A comparison of the resonator sensitivities obtained by the Timoshenko beam model and the EBB model is presented in Table 1. Here, $|S(\omega_i)|_{\rm max}$ denotes the maximum absolute sensitivity for each mode. The relative errors between the sensitivities of the two beam models are given in parentheses. It can be observed from Table 1 that the EBB model overestimates the sensitivity of the resonator, which is due to the neglect of the rotary inertia and shear deformation effects. Furthermore, the relative error between the two models decreases as L/d increases, but increases when the modal number increases. For the method established in the current study, the identification of multi-particle masses requires the detection of higher-order

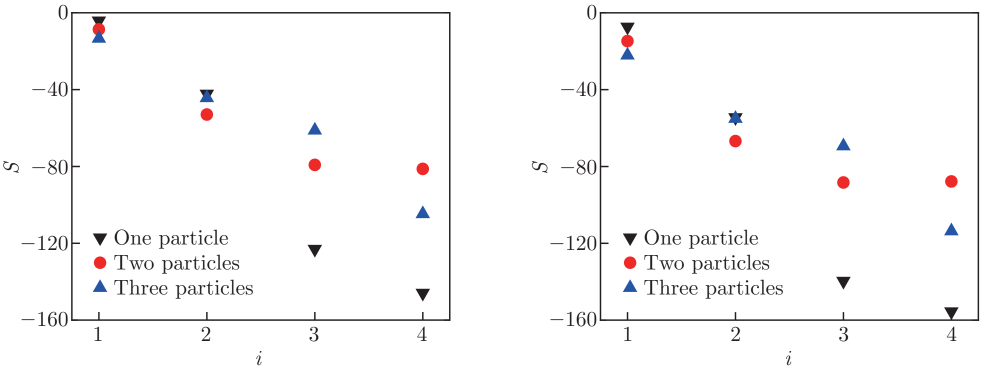

(a) $R_2=0$ (b) $R_2=20$

Fig. 6 Effects of the number of adsorbed particles on the sensitivity when $L = 20d$ and $\lambda = 0$ (color online)

resonant frequencies of the resonator. Therefore, the Timoshenko beam model is essential for improving the accuracy of mass detection.

Table 1 Comparison of the sensitivities between the Timoshenko beam model and the EBB model when $R_2 = 0$ and $\lambda = 0$

Model	L/d	$\lvert S(\omega_1)\rvert_{\max}$	$\lvert S(\omega_2)\rvert_{\max}$	$\lvert S(\omega_3)\rvert_{\max}$	$\lvert S(\omega_4)\rvert_{\max}$
Timoshenko beam	10	26.916 2 (−2.88%)	59.437 9 (−13.14%)	103.518 6 (−22.45%)	147.722 9 (−31.64%)
	20	27.503 7 (−0.75%)	65.838 3 (−3.79%)	123.502 4 (−7.49%)	190.005 5 (−12.08%)
	30	27.618 0 (−0.34%)	67.244 5 (−1.73%)	128.756 3 (−3.55%)	203.207 4 (−5.97%)
	40	27.658 5 (−0.19%)	67.756 5 (−0.99%)	130.765 1 (−2.04%)	208.551 4 (−3.49%)
EBB	–	27.710 9	68.430 6	133.494 6	216.102 4

4.3 Particle detection

Considering a C-C SWCNT resonator sensor with a single adsorbed particle of the relative mass $m_{\mathrm{r}} = 0.001$, the identification of the particle position is illustrated in Fig. 7. Owing to the boundary conditions and the symmetry of the vibration mode, the identifiable range of the particle position is constrained to $\xi_p \in [0.2, 0.5]$. The selection of the nonlocal parameter λ is based on the results given in Ref. [53]. In Fig. 7(a), the case where the particle is adsorbed at $\xi_1 = 0.3$ is displayed. The solid black curve plots the F_2/F_1 ratio as a function of ξ_1, calculated with the left-hand expression of Eq. (41). The dashed red line indicates the G_2/G_1 ratio determined by substituting ω_1 and ω_2 into the right-hand expression of Eq. (41), where ω_1 and ω_2 are obtained by $\det(\boldsymbol{K}) = 0$. The intersection of the solid black curve and dashed red line provides the estimated particle position $\xi_1 = 0.300\,0$. A estimated particle mass of $1.000\,6 \times 10^{-3}$ is then obtained by substituting this positional parameter into Eq. (39), with a 0.06% relative error to the actual particle mass. Similarly, the case where the particle is adsorbed at $\xi_1 = 0.4$ is shown in Fig. 7(b). The intersection of the solid black curve and dashed red line occurs at $\xi_1 = 0.399\,9$. When this estimated position is substituted into Eq. (39), the particle mass is calculated as $1.000\,8 \times 10^{-3}$ with a 0.08% relative error.

Assume that two particles with identical masses of $m_{\mathrm{r}} = 0.001$ are attached to the resonator, and their actual adsorption positions are $\xi_1 = 0.25$ and $\xi_2 = 0.35$, respectively. The identification of the particle positions is illustrated in Fig. 8. In Fig. 8(a), the curved surface shows F_2/F_1 obtained from Eq. (42) as a function of ξ_1 and ξ_2. The plane $G_2/G_1 = 1.625\,0$ is obtained by substituting the resonant frequencies ω_1 and ω_2 of the resonator after particle attachment into Eq. (42). The intersection curve between the surface and plane corresponds to all possible com-

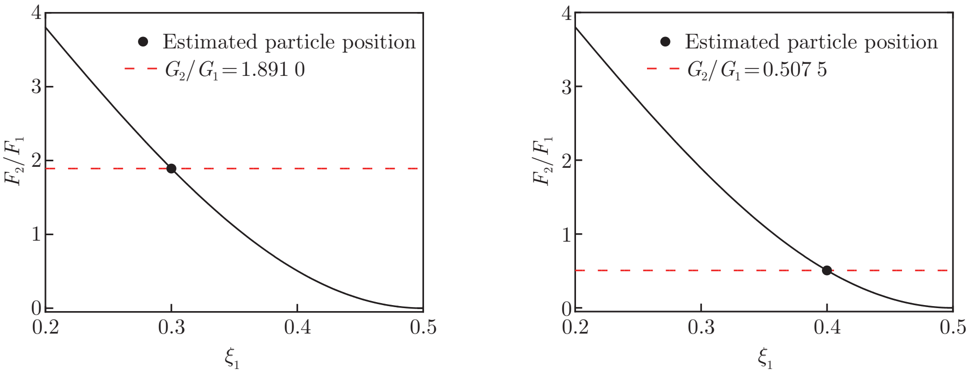

(a) $\xi_1=0.3$ (b) $\xi_1=0.4$

Fig. 7 Position determination of a single particle under the C-C boundary conditions when $L = 40d$, $R_2 = 1$, $\lambda = 1 \times 10^{-4}$, and $m_{\mathrm{r}} = 0.001$ (color online)

binations of particle positions satisfying $F_2/F_1 = G_2/G_1$. Similarly, the surface representing F_3/F_1 and the plane defined by $G_3/G_1 = 0.784\,2$ are shown in Fig. 8(b). The intersection curve indicates possible particle positions satisfying $F_3/F_1 = G_3/G_1$. Projecting the two intersection curves from Figs. 8(a) and 8(b) onto the $\xi_1\xi_2$-plane yields Fig. 8(c). The intersections of these projected curves are $(0.250\,3,\ 0.350\,2)$ and $(0.350\,2,\ 0.250\,3)$, which represent the estimated particle positions. Notably, these two intersections are physically equivalent since the particles have identical masses, and swapping their positions produces identical effects on the resonant frequencies of the resonator. Finally, the estimated relative particle mass $m_{\mathrm{r}} = 9.987\,2 \times 10^{-4}$ with a -0.13% error to the actual particle mass is obtained by substituting either set of the position parameters into Eq. (43).

The identification results of two widely separated particles are illustrated in Fig. 9. The actual adsorption positions of the particles are $\xi_1 = 0.20$ and $\xi_2 = 0.40$. Projecting the intersection lines between the surfaces and planes in Figs. 9(a) and 9(b) onto the $\xi_1\xi_2$-plane yields the results shown in Fig. 9(c). The intersection points of the two curves in Fig. 9(c) are determined as $(0.207\,9,\ 0.402\,9)$ and $(0.402\,9,\ 0.207\,9)$. As discussed on Fig. 8(c), these points represent the estimated particle positions, which are essentially identical except for a transposed order of the particles. Substituting these estimated particle positions into Eq. (43) yields an estimated particle mass of $m_{\mathrm{r}} = 9.729\,9 \times 10^{-4}$, with a -2.70% error compared with the actual mass.

The identification results for the particles with distinct masses under the C-C boundary conditions are presented in Tables 2 and 3. The percentage errors between the estimated and exact particle masses are given in parentheses. As shown in Table 2, the proposed method accurately estimates the particle masses in both single- and multi-particle cases, with minimal errors relative to the exact values. The mass identification results for the dimensionless nonlocal parameter $\lambda = 6.25 \times 10^{-3}$ [50,52] are presented in Table 3. It can be observed from Table 3 that the proposed method is capable of accurately identifying the particle masses for different nonlocal parameters.

4.4 Influence of noise

The resonator-based mass detection is typically affected by noise[54–55]. To evaluate the robustness of the current particle mass identification method in the presence of noise, the following expression for the estimated particle relative mass incorporating noise effects is assumed[34]:

$$m_{\mathrm{r}} = m_{\mathrm{r}}^{\mathrm{exact}} + m_{\mathrm{r}}^{\mathrm{noise}}, \tag{48}$$

where $m_{\mathrm{r}}^{\mathrm{exact}}$ and $m_{\mathrm{r}}^{\mathrm{noise}}$ denote the exact value and noise-affected value of the particle mass, respectively. Substituting Eq. (2) into Eq. (36) under the assumption of Gaussian noise, the

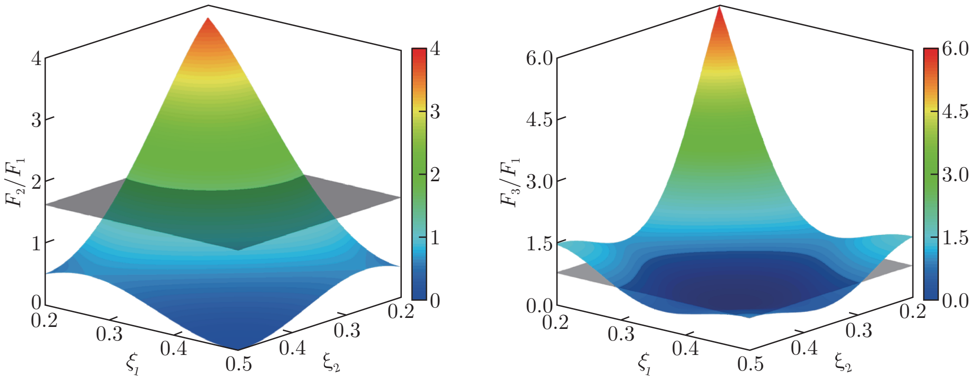

(a) Variation of F_2/F_1 with particle positions ξ_1 and ξ_2

(b) Variation of F_3/F_1 with particle positions ξ_1 and ξ_2

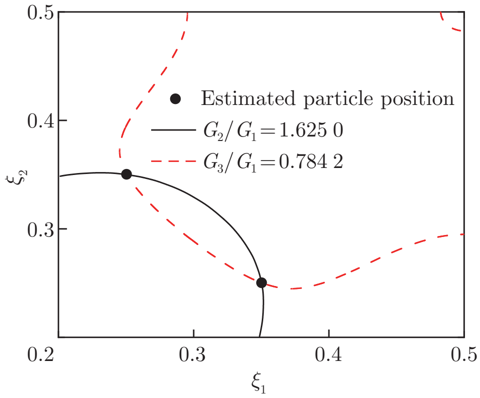

(c) Projection of intersection curves from (a) and (b) onto the $\xi_1\xi_2$-plane

Fig. 8 Position detection of two particles under the C-C boundary conditions when $L = 40d$, $R_2 = 1$, $\lambda = 1\times 10^{-4}$, and $m_{\mathrm{r}} = 0.001$ (color online)

Table 2 Detection of particles with different masses under the C-C boundary conditions when $L = 40d$, $R_2 = 1$, and $\lambda = 1\times 10^{-4}$

Particle	Result	Mass	ξ_1	ξ_2	ξ_3
One particle	Exact	1×10^{-3}	0.3	–	–
	Estimated	$1.000\,6\times 10^{-3}$ (0.06%)	0.300 0	–	–
Two particles	Exact	1×10^{-2}	0.4	–	–
	Estimated	$9.983\,1\times 10^{-3}$ (-0.17%)	0.401 1	–	–
	Exact	1×10^{-3}	0.25	0.35	–
	Estimated	$9.987\,2\times 10^{-4}$ (-0.13%)	0.250 3	0.350 2	–
Three particles	Exact	5×10^{-3}	0.3	0.4	–
	Estimated	$4.973\,3\times 10^{-3}$ (-0.53%)	0.301 3	0.401 8	–
	Exact	1×10^{-3}	0.2	0.3	0.4
	Estimated	$9.957\,4\times 10^{-4}$ (-0.43%)	0.201 4	0.300 5	0.400 7
	Exact	3×10^{-3}	0.3	0.4	0.45
	Estimated	$2.984\,8\times 10^{-3}$ (-0.51%)	0.303 8	0.396 5	0.457 3

resulting equation can be expressed as follows[34]:

$$(m_{\mathrm{r}}^{\mathrm{exact}}+m_{\mathrm{r}}^{\mathrm{noise}})F_i(R_1,\lambda,\xi_1,\xi_2,\xi_3,\cdots,\xi_P)=(1+\chi r_g)G_i(R_1,R_2,R_3,\lambda,\omega_1)+\chi r_g, \tag{49}$$

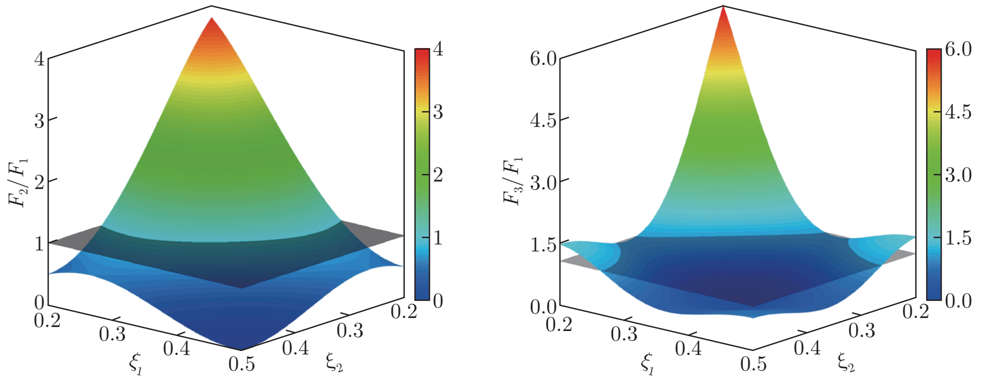

(a) Variation of F_2/F_1 with particle positions ξ_1 and ξ_2

(b) Variation of F_3/F_1 with particle positions ξ_1 and ξ_2

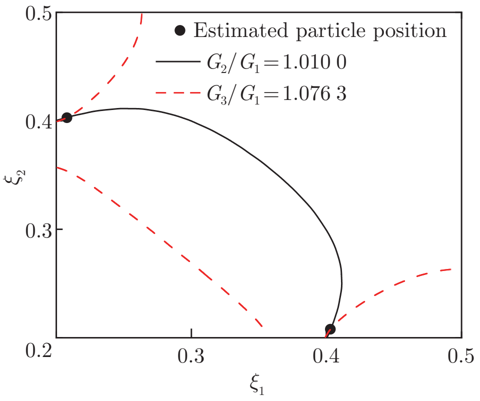

(c) Projection of intersection curves from (a) and (b) onto the $\xi_1\xi_2$-plane

Fig. 9 Position detection of two particles under the C-C boundary conditions when $L = 40d$, $R_2 = 1$, $\lambda = 1 \times 10^{-4}$, and $m_{\rm r} = 0.001$ (color online)

Table 3 Detection of particles with different masses under the C-C boundary conditions when $L = 40d$, $R_2 = 1$, and $\lambda = 6.25 \times 10^{-3}$

Particle	Result	Mass	ξ_1	ξ_2	ξ_3
One particle	Exact	1×10^{-3}	0.35	–	–
	Estimated	$1.001\,0 \times 10^{-3}$ (0.10%)	0.349 9	–	–
Two particles	Exact	6×10^{-3}	0.45	–	–
	Estimated	$6.002\,8 \times 10^{-3}$ (0.05%)	0.450 2	–	–
	Exact	4×10^{-3}	0.25	0.45	–
	Estimated	$3.980\,7 \times 10^{-3}$ (−0.48%)	0.251 4	0.451 6	–
Three particles	Exact	5×10^{-3}	0.28	0.32	–
	Estimated	$4.969\,1 \times 10^{-3}$ (−0.62%)	0.279 8	0.322 6	–
	Exact	2×10^{-3}	0.23	0.33	0.42
	Estimated	$1.991\,0 \times 10^{-3}$ (−0.45%)	0.231 3	0.330 7	0.421 3
	Exact	3×10^{-3}	0.30	0.38	0.46
	Estimated	$2.985\,1 \times 10^{-3}$ (−0.50%)	0.303 8	0.377 7	0.466 2

where χ denotes the magnitude of the Gaussian noise uncertainty, and r_g is a random variable following the standard normal distribution, i.e., $r_g \sim {\rm N}(0, 1)$.

To analyze the effect of the noise uncertainty parameter χ on the particle mass identification, 100 000 samples of r_g are generated for a given χ. The probability density P_χ of the mass ratio $m_{\rm r}^{\rm noise}/m_{\rm r}^{\rm exact}$ is then calculated by substituting r_g into Eq. (49). The relative probability density is defined as $P_\chi/P_\chi^{\max}$, where $P_\chi^{\max}$ is the peak density under the specified uncertainty. The relative probability density distributions for the single-particle identification under the C-C boundary conditions are plotted in Figs. 10(a) and 10(b), respectively. As shown in Fig. 10(a), for a particle with $\xi_1 = 0.4$ under a noise level of $\chi = 1 \times 10^{-4}$, the probability of estimating its mass within a 5% error margin is 70.12%. This probability increases as χ decreases. Consistent with this trend, for a particle with $\xi_1 = 0.2$ under a further reduced noise level of $\chi = 1 \times 10^{-5}$ in Fig. 10(b), the probability increases to 94.32%. In addition, the relative probability density of $m_{\rm r}^{\rm noise}/m_{\rm r}^{\rm exact}$ exhibits a sharp peak near zero as the noise uncertainty decreases. This result indicates that minimizing errors in particle mass identification requires reducing or suppressing noise in the operational environment of the resonator.

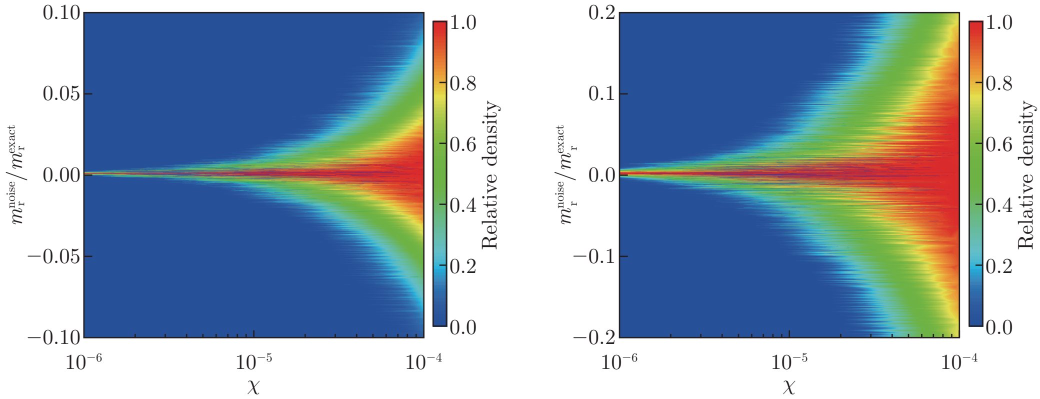

(a) One particle with $\xi_1=0.4$ under the C-C boundary conditions

(b) One particle with $\xi_1=0.2$ under the C-C boundary conditions

Fig. 10 Influence of noise uncertainty χ on the single particle mass identification when $L = 40d$, $\lambda = 1 \times 10^{-4}$, $R_2 = 1$, and $m_{\rm r} = 0.001$ (color online)

The effects of the particle number on the mass identification under different noise uncertainties are investigated in Fig. 11. The relative probability density distributions of $m_{\rm r}^{\rm noise}/m_{\rm r}^{\rm exact}$ for three cases under the C-C boundary conditions are displayed in Figs. 11(a) and 11(b): one particle with $\xi_1 = 0.4$; two particles with $\xi_1 = 0.4$ and $\xi_2 = 0.3$; three particles with $\xi_1 = 0.4$, $\xi_2 = 0.3$, and $\xi_3 = 0.2$. The narrower relative probability density curves observed in multi-particle cases indicate that increasing the number of particles can effectively weaken the effects of noise on the particle mass detection.

5 Conclusions

Based on the nonlocal Timoshenko beam theory, a dynamic model incorporating the thermally induced axial force for the CNT resonator is established in this study. The governing equations are derived with Hamilton's principle. Approximate analytical solutions for the resonant frequencies of the system are obtained with the Galerkin method. The results demonstrate that the resonant frequencies are increased by the axial force but decreased by the nonlocal parameter. Moreover, the number and positions of the adsorbed particles significantly influence the sensitivity of the resonator, with higher-order modes exhibiting greater sensitivity.

To address particle identification, the particle mass and position parameters are decoupled, eliminating the need for the initial mass guesses. The identification process for particles under different boundary conditions is elaborated in detail. The numerical verification confirms that

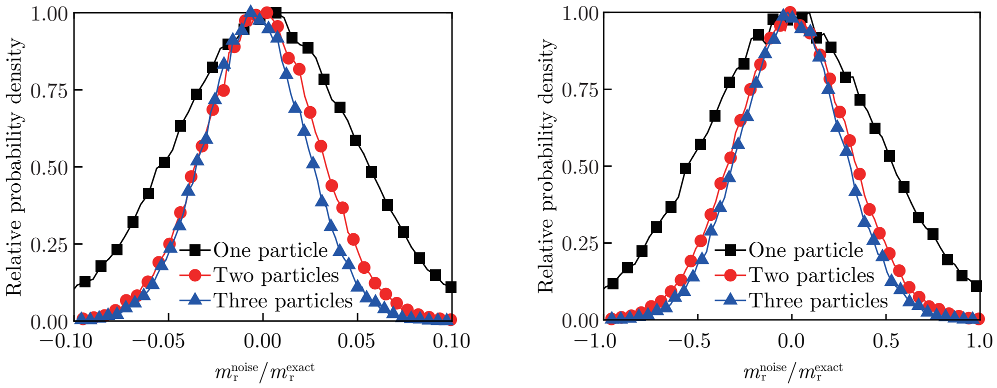

(a) C-C boundary conditions ($\chi=1\times10^{-4}$)   (b) C-C boundary conditions ($\chi=1\times10^{-3}$)

Fig. 11 Relative probability density for different numbers of particles when $L = 40d$, $m_r = 0.001$, and $R_2 = 1$ (color online)

the present method delivers high-quality mass estimation for both single-particle and multi-particle adsorption cases. Furthermore, the performance of the present method under noise disturbances is evaluated, revealing that increasing the number of adsorbed particles enhances the noise resistance of the identification results. This work provides a theoretical foundation and methodology for the high-sensitivity, high-robustness particle detection with CNT resonators in complex environments.

Conflict of interest The authors declare no conflict of interest.

References

[1] IIJIMA, S. Helical microtubules of graphitic carbon. *nature*, **354**(6348), 56–58 (1991)

[2] ARASH, B. and WANG, Q. A review on the application of nonlocal elastic models in modeling of carbon nanotubes and graphenes. *Computational Materials Science*, **51**(1), 303–313 (2012)

[3] POPOV, V. N., VAN DOREN, V. E., and BALKANSKI, M. Elastic properties of single-walled carbon nanotubes. *Physical Review B*, **61**(4), 3078–3084 (2000)

[4] MARTEL, R., DERYCKE, V., LAVOIE, C., APPENZELLER, J., CHAN, K. K., TERSOFF, J., and AVOURIS, P. Ambipolar electrical transport in semiconducting single-wall carbon nanotubes. *Physical Review Letters*, **87**(25), 256805 (2001)

[5] WONG, E. W., SHEEHAN, P. E., and LIEBER, C. M. Nanobeam mechanics: elasticity, strength, and toughness of nanorods and nanotubes. *Science*, **277**(5334), 1971–1975 (1997)

[6] LI, J. J. and ZHU, K. D. Weighing a single atom using a coupled plasmon-carbon nanotube system. *Science and Technology of Advanced Materials*, **13**(2), 025006 (2012)

[7] ZHANG, Y. and ZHAO, Y. P. Mass and force sensing of an adsorbate on a string resonator. *Sensors and Actuators B: Chemical*, **221**, 305–311 (2015)

[8] SAZONOVA, V., YAISH, Y., ÜSTÜNEL, H., ROUNDY, D., ARIAS, T. A., and MCEUEN, P. L. A tunable carbon nanotube electromechanical oscillator. *nature*, **431**(7006), 284–287 (2004)

[9] HÜTTEL, A. K., STEELE, G. A., WITKAMP, B., POOT, M., KOUWENHOVEN, L. P., and VAN DER ZANT, H. S. J. Carbon nanotubes as ultrahigh quality factor mechanical resonators. *Nano Letters*, **9**(7), 2547–2552 (2009)

[10] CHASTE, J., EICHLER, A., MOSER, J., CEBALLOS, G., RURALI, R., and BACHTOLD, A. A nanomechanical mass sensor with yoctogram resolution. *Nature Nanotechnology*, **7**(5), 301–304 (2012)

[11] GEORGANTZINOS, S. K. and ANIFANTIS, N. K. Carbon nanotube-based resonant nanomechanical sensors: a computational investigation of their behavior. *Physica E: Low-dimensional Systems and Nanostructures*, **42**(5), 1795–1801 (2010)

[12] HSU, J. C., LEE, H. L., and CHANG, W. J. Thermal buckling of double-walled carbon nanotubes. *Journal of Applied Physics*, **105**(10), 103512 (2009)

[13] KHANIKI, H. B. On vibrations of nanobeam systems. *International Journal of Engineering Science*, **124**, 85–103 (2018)

[14] ZHANG, Y. and ZHAO, Y. P. Measuring the nonlocal effects of a micro/nanobeam by the shifts of resonant frequencies. *International Journal of Solids and Structures*, **102-103**, 259–266 (2016)

[15] İNCE, A. and ERKOÇ, Ş. Molecular-dynamics simulations of silicene nanoribbons under strain. *Physica Status Solidi B: Basic Research*, **249**, 74–81 (2012)

[16] HEIDARY, Z., RAMEZANI, S. R., and MOJRA, A. Exploring the benefits of functionally graded carbon nanotubes (FG-CNTs) as a platform for targeted drug delivery systems. *Computer Methods and Programs in Biomedicine*, **238**, 107603 (2023)

[17] MIKHASEV, G., RADI, E., and MISNIK, V. Modeling pull-in instability of CNT nanotweezers under electrostatic and van der Waals attractions based on the nonlocal theory of elasticity. *International Journal of Engineering Science*, **195**, 104012 (2024)

[18] ANH, V. T. T., DAT, N. D., NGUYEN, P. D., and DUC, N. D. A nonlocal higher-order shear deformation approach for nonlinear static analysis of magneto-electro-elastic sandwich micro/nanoplates with FG-CNT core in hygrothermal environment. *Aerospace Science and Technology*, **147**, 109069 (2024)

[19] THAI, H. T. A nonlocal beam theory for bending, buckling, and vibration of nanobeams. *International Journal of Engineering Science*, **52**, 56–64 (2012)

[20] ERINGEN, A. C. On differential equations of nonlocal elasticity and solutions of screw dislocation and surface waves. *Journal of Applied Physics*, **54**(9), 4703–4710 (1983)

[21] WANG, Q. Y. and ZHANG, Z. L. Chaotic vibration of a curved CNT conveying magnetic fluid in the thermo-magnetic field considering the surface effects. *Thin-Walled Structures*, **202**, 112047 (2024)

[22] ZENG, Z., LU, K., WANG, X. F., and HU, R. C. Stochastic analysis for the embedded single-walled carbon nanotube under random vibrations. *International Journal of Structural Stability and Dynamics*, **25**(8), 2550083 (2025)

[23] MAWPHLANG, B. R. K. L. L. and PATRA, P. K. Study of the large bending behavior of CNTs using LDTM and nonlocal elasticity theory. *International Journal of Non-Linear Mechanics*, **166**, 104828 (2024)

[24] LI, C., CHEN, R. J., LI, C., and QING, H. Two-phase nonlocal integral model with bi-Helmholtz kernel for free vibration analysis of multi-walled carbon nanotubes considering size-dependent van der Waals forces. *Applied Mathematics and Mechanics* (*English Edition*), **46**(11), 2095–2114 (2025) https://doi.org/10.1007/s10483-025-3313-8

[25] KANG, D. K., YANG, H. I., and KIM, C. W. Geometrically nonlinear dynamic behavior on detection sensitivity of carbon nanotube-based mass sensor using finite element method. *Finite Elements in Analysis and Design*, **126**, 39–49 (2017)

[26] ALI-AKBARI, H. R., CEBALLES, S., and ABDELKEFI, A. Nonlinear performance analysis of forced carbon nanotube-based bio-mass sensors. *International Journal of Mechanics and Materials in Design*, **15**(2), 291–315 (2019)

[27] CEBALLES, S., SAUNDERS, B. E., and ABDELKEFI, A. Nonlocal Timoshenko modeling effectiveness for carbon nanotube-based mass sensors. *European Journal of Mechanics-A/Solids*, **92**, 104462 (2022)

[28] ZHANG, Y. and ZHAO, Y. P. Detecting the mass and position of an adsorbate on a drum resonator. *Proceedings of the Royal Society A: Mathematical, Physical and Engineering Sciences*, **470**(2170), 20140418 (2014)

[29] HEINRICH, S. M. and DUFOUR, I. Toward higher-order mass detection: influence of an adsorbate's rotational inertia and eccentricity on the resonant response of a Bernoulli-Euler cantilever beam. *Sensors*, **15**(11), 29209–29232 (2015)

[30] LI, X. F., TANG, G. J., SHEN, Z. B., and LEE, K. Y. Resonance frequency and mass identification of zeptogram-scale nanosensor based on the nonlocal beam theory. *Ultrasonics*, **55**, 75–84 (2015)

[31] YAO, L. Z., WANG, T., JIANG, C. L., ZHAO, Q., SUI, Y., LU, Y., WANG, Y. K., SUN, Y., CONG, Z. C., and DONG, T. J. Multi-particle sorting using signals from particles trapped by single optical fiber tweezers. *Optical Fiber Technology*, **88**, 103994 (2024)

[32] ZHAO, L., WANG, F., ZHANG, Y. L., and ZHAO, X. Z. Theoretical study on the dynamic behavior of a plate-like micro-cantilever with multiple particles attached. *PLoS One*, **11**(3), e0151821 (2016)

[33] DOHN, S., SCHMID, S., AMIOT, F., and BOISEN, A. Position and mass determination of multiple particles using cantilever based mass sensors. *Applied Physics Letters*, **97**(4), (2010)

[34] WEI, C. X. and ZHANG, Y. Mass identification of multiple particles on a doubly clamped resonator. *Sensors and Actuators B: Chemical*, **360**, 131682 (2022)

[35] MA, S. J., LI, M. X., WANG, S. L., LIU, H., WANG, H., REN, L., HUANG, M. H., and ZHANG, X. W. Multiple particle identification by sequential frequency-shift measurement of a micro-plate. *International Journal of Mechanical Sciences*, **231**, 107587 (2022)

[36] JENSEN, K., KIM, K., and ZETTL, A. An atomic-resolution nanomechanical mass sensor. *Nature Nanotechnology*, **3**(9), 533–537 (2008)

[37] ZHANG, Y. Frequency spectra of nonlocal Timoshenko beams and an effective method of determining nonlocal effect. *International Journal of Mechanical Sciences*, **128-129**, 572–582 (2017)

[38] GARCIA-SANCHEZ, D., SAN PAULO, A., ESPLANDIU, M. J., PEREZ-MURANO, F., FORRÓ, L., AGUASCA, A., and BACHTOLD, A. Mechanical detection of carbon nanotube resonator vibrations. *Physical Review Letters*, **99**(8), 085501 (2007)

[39] REDDY, J. N. Nonlocal theories for bending, buckling and vibration of beams. *International Journal of Engineering Science*, **45**(2), 288–307 (2007)

[40] WANG, Q. and WANG, C. M. The constitutive relation and small scale parameter of nonlocal continuum mechanics for modelling carbon nanotubes. *Nanotechnology*, **18**(7), 075702 (2007)

[41] ZHANG, Y. and LIU, Y. Detecting both the mass and position of an accreted particle by a micro/nano-mechanical resonator. *Sensor*, **14**(9), 16296–16310 (2014)

[42] ZHANG, Y. Detecting the stiffness and mass of biochemical adsorbates by a resonator sensor. *Sensors and Actuators B: Chemical*, **202**, 286–293 (2014)

[43] BENZAIR, A., TOUNSI, A., BESSEGHIER, A., HEIRECHE, H., MOULAY, N., and BOUMIA, L. The thermal effect on vibration of single-walled carbon nanotubes using nonlocal Timoshenko beam theory. *Journal of Physics D: Applied Physics*, **41**(22), 225404 (2008)

[44] AVSEC, J. and OBLAK, M. Thermal vibrational analysis for simply supported beam and clamped beam. *Journal of Sound and Vibration*, **308**(3), 514–525 (2007)

[45] YAO, X. H. and HAN, Q. Investigation of axially compressed buckling of a multi-walled carbon nanotube under temperature field. *Composites Science and Technology*, **67**(1), 125–134 (2007)

[46] WANG, J. and ZHANG, Y. Mass detection based on the 3:1 internal resonance in a piezoelectric laminated microbeam resonator sensor. *Nonlinear Dynamics*, **113**(17), 22625–22649 (2025)

[47] ZHANG, Y. Eigenfrequency computation of beam/plate carrying concentrated mass/spring. *Journal of Vibration and Acoustics*, **133**(2), 021006 (2011)

[48] RAMOS, D., TAMAYO, J., MERTENS, J., CALLEJA, M., and ZABALLOS, A. Origin of the response of nanomechanical resonators to bacteria adsorption. *Journal of Applied Physics*, **100**(10), 106105 (2006)

[49] MCCAIG, H. C., MYERS, E., LEWIS, N. S., and ROUKES, M. L. Vapor sensing characteristics of nanoelectromechanical chemical sensors functionalized using surface-initiated polymerization. *Nano Letters*, **14**(7), 3728–3732 (2014)

[50] DUAN, W. H., WANG, C. M., and ZHANG, Y. Y. Calibration of nonlocal scaling effect parameter for free vibration of carbon nanotubes by molecular dynamics. *Journal of Applied Physics*, **101**(2), 024305 (2007)

[51] WANG, C. M., ZHANG, Y. Y., and HE, X. Q. Vibration of nonlocal Timoshenko beams. *Nanotechnology*, **18**(10), 105401 (2007)

[52] ZHANG, Y. Y., WANG, C. M., and TAN, V. B. C. Assessment of Timoshenko beam models for vibrational behavior of single-walled carbon nanotubes using molecular dynamics. *Advances in Applied Mathematics and Mechanics*, **1**(1), 89–106 (2009)

[53] CEBALLES, S. and ABDELKEFI, A. Uncertainty analysis and stochastic characterization of carbon nanotube-based mass sensor with multiple deposited nanoparticles. *Sensors and Actuators A: Physical*, **332**, 113182 (2021)

[54] HUA, M. J. and WU, Y. Bifurcation in most probable phase portraits for a bistable kinetic model with coupling Gaussian and non-Gaussian noises. *Applied Mathematics and Mechanics* (*English Edition*), **42**(12), 1759–1770 (2021) https://doi.org/10.1007/s10483-021-2804-8

[55] LIU, Z., SONG, X. M., and ZHANG, M. A packet-dropping fusion Kalman filter algorithm based on non-Gaussian noise estimation. *Mechanical Systems and Signal Processing*, **228**, 112457 (2025)

Appendix A

The linear governing equation for the resonator under tension ($R_2 > 0$) is given by

$$\varphi'''' - R_2\varphi'' - \omega^2\varphi = 0. \tag{A1}$$

The C-C and clamped-free (C-F) boundary conditions are governed by

$$\text{C-C: } \varphi|_{\xi=0,1} = 0, \quad \left.\frac{\mathrm{d}\varphi}{\mathrm{d}\xi}\right|_{\xi=0,1} = 0, \tag{A2}$$

$$\text{C-F: } \varphi|_{\xi=0} = 0, \quad \left.\frac{\mathrm{d}\varphi}{\mathrm{d}\xi}\right|_{\xi=0} = 0, \quad \left.\frac{\mathrm{d}^2\varphi}{\mathrm{d}\xi^2}\right|_{\xi=1} = 0, \quad \left.\Big(R_2\frac{\mathrm{d}\varphi}{\mathrm{d}\xi} - \frac{\mathrm{d}^3\varphi}{\mathrm{d}\xi^3}\Big)\right|_{\xi=1} = 0. \tag{A3}$$

The solution to Eq. (A1) is given in the following form:

$$\varphi = C_1\cosh(f_1\xi) + C_2\sinh(f_1\xi) + C_3\cos(f_2\xi) + C_4\sin(f_2\xi), \tag{A4}$$

$$f_1 = \sqrt{\frac{R_2 + \sqrt{R_2^2 + 4\omega^2}}{2}}, \quad f_2 = \sqrt{\frac{-R_2 + \sqrt{R_2^2 + 4\omega^2}}{2}}, \tag{A5}$$

where C_1, C_2, C_3, and C_4 are undetermined constants. By substituting Eq. (A4) into Eq. (A2), the following system of equations is obtained:

$$\begin{cases} C_1 + C_3 = 0, \\ C_2 f_1 + C_4 f_2 = 0, \\ C_1\cosh f_1 + C_2\sinh f_1 + C_3\cos f_2 + C_4\sin f_2 = 0, \\ C_1 f_1\sinh f_1 + C_2 f_1\cosh f_1 - C_3 f_2\sin f_2 + C_4 f_2\cos f_2 = 0. \end{cases} \tag{A6}$$

Based on Eq. (A6), the mode shape of the system under C-C boundary conditions can be written in the following form:

$$\begin{aligned} \varphi =& C_1\Big(\cosh(f_1\xi) + \frac{f_1\cosh f_1 - f_1\cos f_2}{f_2\sinh f_1 - f_1\sin f_2}\sin(f_2\xi)\Big) \\ &- C_1\Big(\cos(f_2\xi) + \frac{f_2\cosh f_1 - f_2\cos f_2}{f_2\sinh f_1 - f_1\sin f_2}\sinh(f_1\xi)\Big). \end{aligned} \tag{A7}$$

By setting the determinant of the coefficient matrix in Eq. (A6) to zero, the frequency equation of the system under C-C boundary conditions is derived as follows:

$$2f_1 f_2(\cosh f_1\cos f_2 - 1) - (f_1^2 - f_2^2)\sinh f_1\sin f_2 = 0. \tag{A8}$$

All the eigenfrequencies of the system can be obtained from Eq. (A8). The corresponding mode shape is then determined by substituting each eigenfrequency into Eq. (A7). Similarly, the mode shape and frequency equation of the system under the C-F conditions are derived by substituting Eq. (A4) into Eq. (A3), as follows:

$$\begin{aligned}\varphi &= C_1\Big(\cosh(f_1\xi) + \frac{f_1^2\cosh f_1 + f_2^2\cos f_2}{f_1 f_2\sinh f_1 + f_2^2\sin f_2}\sin(f_2\xi)\Big)\\ &\quad - C_1\Big(\cos(f_2\xi) + \frac{f_1^2\cosh f_1 + f_2^2\cos f_2}{f_1^2\sinh f_1 + f_1 f_2\sin f_2}\sinh(f_1\xi)\Big),\end{aligned} \tag{A9}$$

$$\begin{aligned}&f_1^4 + f_2^4 + (f_2^2 - f_1^2)R_2 + (2f_1^2 f_2^2 + f_1^2 R_2 - f_2^2 R_2)\cosh f_1\cos f_2\\ &+ (f_1 f_2^3 - f_1^3 f_2 + 2f_1 f_2 R_2)\sinh f_1\sin f_2 = 0.\end{aligned} \tag{A10}$$

The linear governing equation for the resonator under compression ($R_2 < 0$) is given by

$$\varphi'''' + R_2\varphi'' - \omega^2\varphi = 0. \tag{A11}$$

The boundary conditions for the C-C beam are still expressed by Eq. (A2), whereas those for the C-F beam are rewritten as follows:

$$\varphi|_{\xi=0} = 0, \quad \frac{\mathrm{d}\varphi}{\mathrm{d}\xi}\Big|_{\xi=0} = 0, \quad \frac{\mathrm{d}^2\varphi}{\mathrm{d}\xi^2}\Big|_{\xi=1} = 0, \quad \Big(R_2\frac{\mathrm{d}\varphi}{\mathrm{d}\xi} + \frac{\mathrm{d}^3\varphi}{\mathrm{d}\xi^3}\Big)\Big|_{\xi=1} = 0. \tag{A12}$$

The solution to Eq. (A11) is given in the following form:

$$\varphi = C_1\cosh(f_2\xi) + C_2\sinh(f_2\xi) + C_3\cos(f_1\xi) + C_4\sin(f_1\xi). \tag{A13}$$

By following the same procedure as for the tension case, the eigenfrequencies and mode shapes of the resonator under compression can be obtained.